Dipole–dipole-interaction-assisted self-assembly of quantum dots for highly efficient light-emitting diodes

Huaiyu Xu [1,2,9], Jiaojiao Song[3,9], Penghao Zhou[3,9], Yang Song [1,2,9], Jian Xu[4,9], Huaibin Shen [3 ✉], Shucheng Fang[1,2], Yan Gao[3], Zhenjiang Zuo[1,2], João M. Pina [4], Oleksandr Voznyy [5], Chunming Yang [6], Yongfeng Hu [7], Jun Li [8], Jiangfeng Du [1,2 ✉], Edward H. Sargent [4 ✉] & Fengjia Fan [1,2 ✉]

The external quantum efficiency of state-of-the-art quantum dot light-emitting diodes is limited by the low photon out-coupling efficiency. Light-emitting diodes using oriented nanostructures such as nanorods, nanoplatelets and dot-in-disc nanocrystals favour photon out-coupling; however, their internal quantum efficiency is often compromised and thus achieving a net gain has proved challenging. Here we report isotropic-shaped quantum dots featuring a mixed-crystallographic structure composed of wurtzite and zinc blende phases. The wurtzite phase promotes dipole– dipole interactions that orient quantum dots in solution-processed films, whereas the zinc blende phase helps lift the electronic state degeneracy to enable directional light emission. These combined features improve photon out-coupling without compromising internal quantum efficiency. Fabricated light-emitting diodes exhibit an external quantum efficiency of 35.6% and can be continuously operated with an initial brightness of 1,000 cd m^{-2} for 4.5 years with a minimal performance loss of about 5%.

External quantum efficiencies (EQEs) in quantum dot (QD) light-emitting diodes (LEDs) are now approaching the limits set by finite photon out-coupling: typically, fewer than 30% of generated photons escape, with the balance trapped inside devices[1–6]. Orienting transition dipoles to increase photon emission perpendicular to the device substrate offers the prospect of improved out-coupling efficiency[7–10], it requires us to orient the crystallographic axis of individual nanocrystals possessing directional light emission. This has been demonstrated in anisotropic nanocrystals such as nanoplatelets[11,12], nanorods[13] and

QDs with flat exposed facets[14,15], where van der Waals interactions are considered to be the main driving force; however, LEDs employing such anisotropic nanoemitters suffer from low radiative recombination efficiency, so the gain in photon out-coupling is more than offset by the loss in internal quantum efficiency. A feasible out-coupling strategy to enable EQEs above 30% in planar QD-LED is yet to be demonstrated.

Here, by increasing the ionicity of the QDs, we can enhance the dipole–dipole interactions among quasispherical QDs and uniformly orient them in solution-processed films. At the same time,

[1]CAS Key Laboratory of Microscale Magnetic Resonance and School of Physical Sciences, University of Science and Technology of China, Hefei, China. [2]Hefei National Laboratory, University of Science and Technology of China, Hefei, China. [3]Key Laboratory for Special Functional Materials of Ministry of Education, National & Local Joint Engineering Research Center for High-efficiency Display and Lighting Technology, Henan University, Kaifeng, China. [4]Department of Electrical and Computer Engineering, University of Toronto, Toronto, Ontario, Canada. [5]Department of Physical and Environmental Sciences, University of Toronto Scarborough, Toronto, Ontario, Canada. [6]Shanghai Synchrotron Radiation Facility, Shanghai Advanced Research Institute, Chinese Academy of Sciences, Shanghai, China. [7]Sinopec Shanghai Research Institute of Petrochemical Technology, Shanghai, China. [8]Frontiers Science Center for Transformative Molecules, Shanghai Jiao Tong University, Shanghai, China. [9]These authors contributed equally: Huaiyu Xu, Jiaojiao Song, Penghao Zhou, Yang Song, Jian Xu. ✉e-mail: shenhuaibin@henu.edu.cn; djf@ustc.edu.cn; ted.sargent@utoronto.ca; ffj@ustc.edu.cn
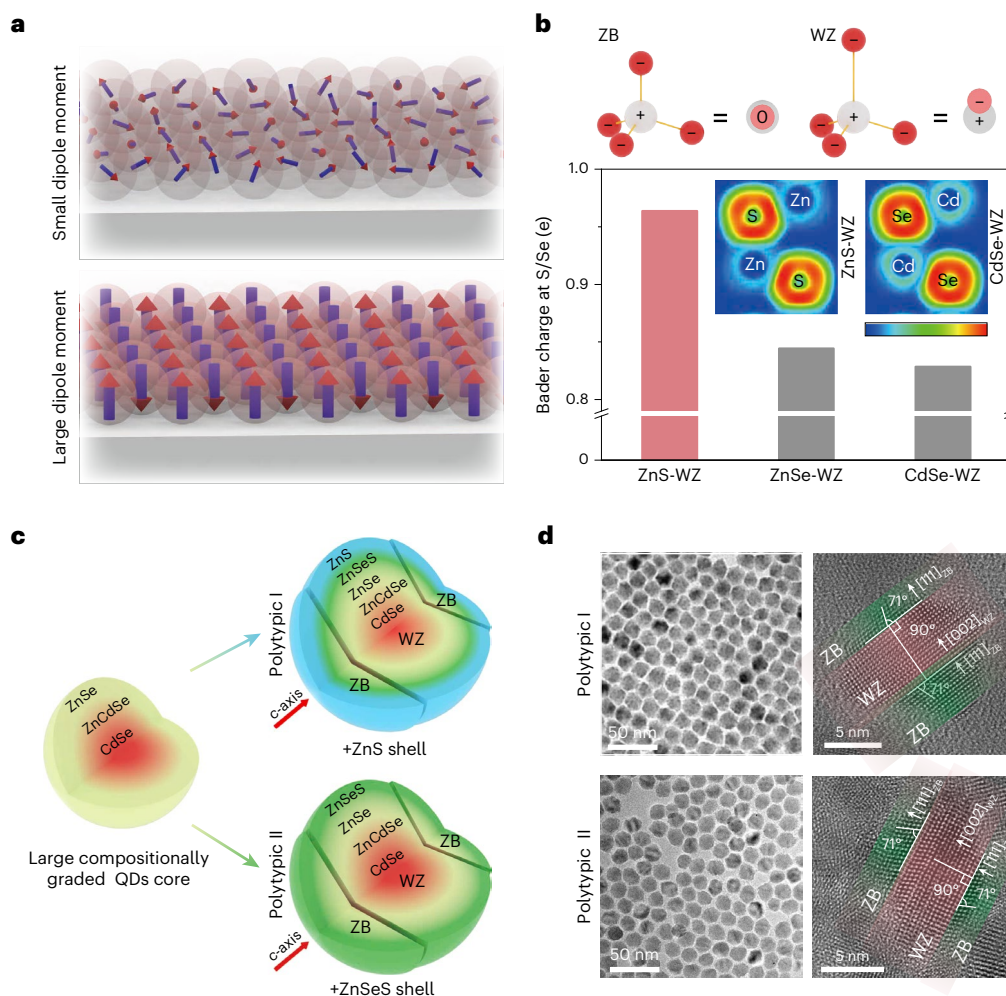
Fig. 1 | Synthesis of polytypic QDs with large permanent dipole moments.
a, Schematic illustrating the role of permanent dipole moments in producing the antiparallel orientation of QDs. **b**, The origin of the permanent dipole in the WZ structure, and calculated Bader charges for S/Se in ZnS, ZnSe and CdSe compounds; a larger Bader charge indicates stronger ionicity. The insets show the electron localization functions of wurtzite ZnS and CdSe. **c**, Synthesis schematic for two types of polytypic QDs with ZnS-rich and -poor outermost shells. **d**, TEM and HRTEM images viewed along the $[110]_{WZ}$ and $[110]_{ZB}$ axes of polytypic I and II QDs.

the individual QDs are featured with a wurtzite (WZ)/zinc blende (ZB) mixed-crystallographic phase, allowing directional light emission. By combining the uniformly oriented polytypic QDs with judiciously engineered electron and hole injection, we achieve EQEs up to 35.6% in QD-LEDs—a value remarkably higher than the maximum achievable value for isotropic emitters. The high EQEs allow our QD-LEDs to be operated with reduced Joule heat and driving voltage, leading to a long operating lifetime (extrapolated T_{95} at 1,000 cd m^{-2} of over 40,000 h).

Results and discussion

Aside from the van der Waals forces, the dipole–dipole interaction is another important force that affects the self-assembly of nanocrystals[16–18]. Such interactions allow spontaneous antiparallel alignment of the crystallographic axis of nanocrystals[19], if the direction of the dipole moments is aligned to a certain crystallographic axis and the magnitude is large enough to overcome the thermal disturbance (Fig. 1a).

In ZB QDs, the direction of the dipole moment is independent of the crystallographic axis because the permanent dipoles are caused by electric charges trapped at surface defect states[20]. Consequently, dipole–dipole interactions do not determine the orientation of ZB QDs regardless of the dipole–dipole interaction strength. By contrast, for the WZ counterpart, the permanent dipole moment parallel to the

c-axis originates from the displacement of atoms in this direction[20]; as a result, WZ-QDs orient with their $[001]_{WZ}$ axis (that is, the c-axis of the WZ structure) perpendicular to the substrate, if the dipole–dipole interaction is strong enough (Fig. 1a).

The magnitude of the dipole moment depends on the QD's size and chemical composition: more ionic compounds lead to larger permanent dipole moments[20]. Bader charge calculations suggest that ZnS is more ionic than ZnSe and CdSe (Fig. 1b); however, the stable phase of ZnS below 1,000 °C is ZB[21], which does not facilitate oriented self-assembly. Furthermore, conventional large QDs are usually synthesized by slowly growing thick shells on small cores to eliminate trap states[22]. As a result, the shell material tends to crystallize in the thermodynamically stable (ZB) phase, posing challenges to the growth of WZ-ZnS shells.

In this work, instead of growing thick shells on small cores, we synthesized CdZnSe with large core diameters (13.5 nm) (Supplementary Fig. 1, see Methods for details) via a fast nucleation process. This enabled us to achieve a high-purity WZ structure (Supplementary Fig. 1). We then used the WZ CdZnSe cores as structural templates to grow the WZ ZnS shell epitaxially. We obtain QDs with sufficient WZ ZnS co-existing with the ZB counterpart. The WZ portion of the heterostructure provides the desired large permanent dipole moment that facilitates the QD orientation, and the ZB component influences the
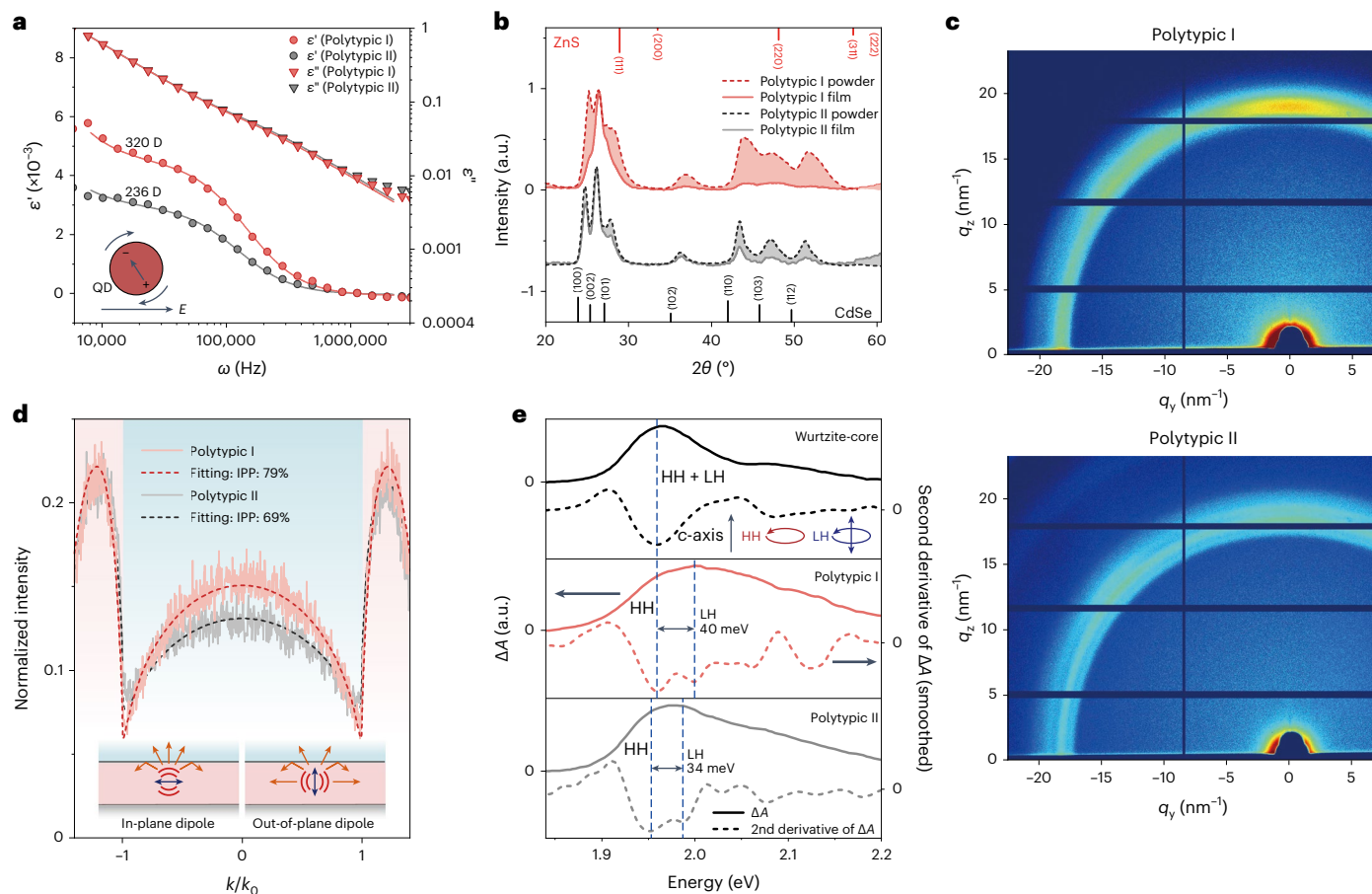
Fig. 2 | Characterization of polytypic QDs and their orientation. a, Dielectric spectra of polytypic I (red) and polytypic II (grey) QDs dispersed in decalin. The inset shows a measurement schematic of the dipole moment magnitude obtained based on the variation in permittivity, the result of dipole rotation at the relaxation frequency of the alternating electric field (see Methods for details). By fitting the real (ε', dots) and imaginary (ε'', triangles) parts of the permittivity, we obtain dipole moments of 320 and 236 D for polytypic I and II QDs, respectively. **b**, X-ray diffraction of powder and film samples of polytypic I (red) and polytypic II (grey) QDs. The bulk WZ CdSe and ZB ZnS powder XRD data (powder diffraction file: 08-0459 and 80-0020) are provided for comparison. The diffraction peaks of the polytypic I QDs appear at larger angles than their counterparts, indicating more ZnS content in the QDs. **c**, GIWAXS patterns of polytypic I and II QD films. **d**, Experimental BFP profiles of polytypic I (red) and polytypic II (grey) QDs, indicating in-plane dipole proportions (IPPs) of 79% and 69%, respectively. **e**, The bleach signals from transient absorption measurements. The second derivatives of the bleach spectra of WZ-core and polytypic I QDs allow us to quantify the splitting energy (40 meV). The dashed line highlights the transition peak positions.

electronic structure compared with that of pure WZ QDs[23]—a strategy that aims to promote directional emission from each nanocrystal.

To investigate the effect of ionicity on the strength of dipole–dipole interactions and the orientation of QDs, we adjusted the ZnSe/ZnS ratio during shell growth and prepared two types of polytypic QDs: one had a ZnS-rich (polytypic I) outermost shell; the other had a ZnSe-rich (polytypic II) outermost shell (Fig. 1c and Supplementary Fig. 2).

Using a transmission electron microscope (TEM) (Fig. 1d), we observe that the average sizes (17 ± 0.5 nm) of the polytypic I and II QDs are similar. High-resolution transmission electron microscopy (HRTEM) (Fig. 1d) reveals that each class of QD possesses a sandwich-like polycrystalline structure: on the top and bottom of each dot is the ZB phase, revealed by $(111)_{ZB}$ and $(002)_{ZB}$ lattice fringes; with materials in-between evincing $(002)_{WZ}$ and $(\bar{1}10)_{WZ}$ lattice fringes.

Dipole moment measurements

To quantify the magnitude of the permanent dipole moments, we measured the dielectric spectra of QD dispersions[24] (see Methods for details). We found that the dipole moment of polytypic I QDs (320 D) is larger than that of polytypic II QDs (236 D) (Fig. 2a). Considering that these have similar average particle sizes and crystal structures, we attribute

the increase in the permanent dipole moment in polytypic I QDs to the stronger ionicity of ZnS. Density functional theory (DFT) calculations estimate dipole moments of 195 D and 136 D for polytypic I and II QDs with a diameter of 8 nm, respectively; the ratio of these figures (~1.4) shows good agreement between computation and experiments.

Orientation of QDs in film

To characterize whether larger permanent dipole moments enhance dipole–dipole interactions and promote the antiparallel arrangement of the QDs (Fig. 1a), we performed comparative X-ray diffraction (XRD) studies on powder versus film samples. The reference powder samples were finely ground to eliminate preferential orientation. The characteristic peak positions from the powders of both classes of QDs match those of WZ CdZnSeS. We attribute the additional diffraction peaks at 27° (Fig. 2b) to the $(111)_{ZB}$ crystalline facet of the ZB phase, consistent with the polytypic structure. The XRD pattern of polytypic I (with a thick ZnS shell) QD films greatly differs from that of the powder samples. We observed a remarkable increase in the $(002)_{WZ}$ (Fig. 2b) diffraction peak intensity, indicating that the $[002]_{WZ}$ axes (that is, the c-axis of WZ structure) are uniformly oriented perpendicular to the substrate. The polytypic II QDs (with a ZnSe-rich shell) adopt a less favourable orientation. We also performed grazing incidence wide-angle X-ray
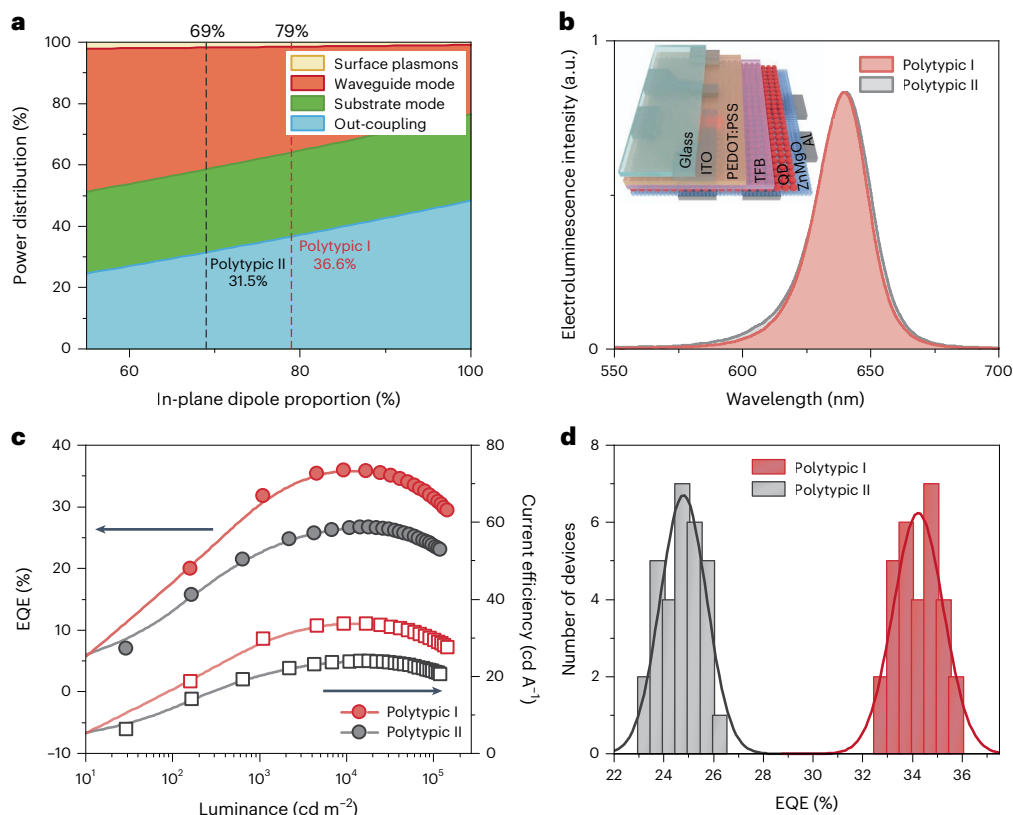
Fig. 3 | Simulations and experimental studies of QD-LED devices. a, Power distribution in out-coupled and trapped modes (that is, substrate, waveguide and surface plasmons modes) as a function of in-plane dipole proportions. The two dashed lines highlight the power distribution QD-LEDs with 79% and 69% in-plane dipole proportions, and theoretical out-coupling efficiencies of 36.6% and 31.5%, respectively. **b**, Electroluminescence spectra of polytypic QD-LEDs with emission peaks at 640 nm. The inset shows a schematic of the QD-LED architecture. **c**, EQEs (solid circles) and current efficiencies (open squares) versus luminance. **d**, Histogram of peak EQEs measured from 30 devices.

scattering (GIWAXS) measurements (Fig. 2c and Supplementary Fig. 3)[10,25]. Consistent with the XRD analysis, we observed a uniform Debye−Scherrer ring corresponding to the $(002)_{WZ}$ crystalline facet of polytypic II QD films in the GIWAXS image; furthermore, cuts along the q_z and q_y axes in the GIWAXS diffractogram resemble each other, indicating a random orientation of nanocrystals. The preferential orientation of the $(002)_{WZ}$ facet is parallel to the substrate in the GIWAXS image of the polytypic I QD films, together with the difference between the cuts along the q_z and q_y axes (Supplementary Fig. 3), further confirms the anisotropic nanocrystal orientation.

Given the similarities between polytypic I and II QDs in their size, shape and crystallographic structure, we attribute the variations to the unique ionicities of the shells. We further synthesized two more QDs with similar sizes and adjusted the ZnSe/ZnS ratio to be in-between those of polytypic I and II QDs, we observed a progressive increase in permanent dipole moment and degree of QD orientation (Supplementary Fig. 4 and 5). These results further suggest that the orientation is caused by dipole−dipole interactions among QDs. We also found that the uniformity of orientation is mainly determined by the QD type, and it is not sensitive to the film fabrication conditions, such as spin-coating speed and substrate size (Supplementary Figs. 6 and 7).

Directional light emission from single QDs

Enhanced light extraction in films requires not only consistent orientation but also directional light emission from the constituent QDs. The band-edges of II–VI QDs are degenerate manifolds, with heavy hole (HH) excitons preferentially emitting along the *c*-axis and light hole (LH) excitons emitting almost isotropically[26]. In spherical WZ QDs, the HH and LH degeneracy is lifted by the internal crystal field along

the *c*-axis[26,27], leaving HH as the ground state and enabling directional emission along the *c*-axis.

To quantify the splitting energy between HH and LH excitons experimentally, we performed ultrafast transient absorption measurements and analysed the transition peaks from the bleach spectra. From the second derivatives, splittings of 40 meV and 34 meV (Fig. 2e) are observed in polytypic I and II QDs, respectively. As seen in conventional WZ QDs[22,28], for WZ CdZnSe QDs, the splitting is too small to be resolved. The finding here reveals that polytypic QDs not only inherit the internal crystal field of the WZ structure, but also benefit from WZ-ZB stacking disorder, leading to an enlarged HH and LH splitting. This agrees with DFT studies that reveal a splitting of 26 meV in pure WZ QDs and an increased splitting of 38 meV in polytypic QDs (Supplementary Fig. 8). It is worth noting that the splitting of polytypic II QDs (34 meV) is, in principle, big enough to allow preferential photon emission along the *c*-axis, but the emission of their films resembles that of isotropic emitters because of lack in crystallography orientations. Past studies also show that an asymmetric shell and anisotropic lattice mismatch generates anisotropic strain in QDs, lifting the HH and LH degeneracy[22,28]. However, in the polytypic QDs here, anisotropic strain is unlikely to cause the enlarged splitting as the QDs are near-isotropic in shape. Furthermore, unlike ZnSe shells that stress CdSe cores anisotropically along different crystallographic axes[22], ZnS exerts only uniform strain on CdSe because of the uniform lattice matching along all crystallographic directions (ICSD nos. 657411 and 600840).

Enhanced light extraction in QD films

We then sought to investigate whether the uniform orientation enables increased photon extraction from QD films. We used back-focal plane
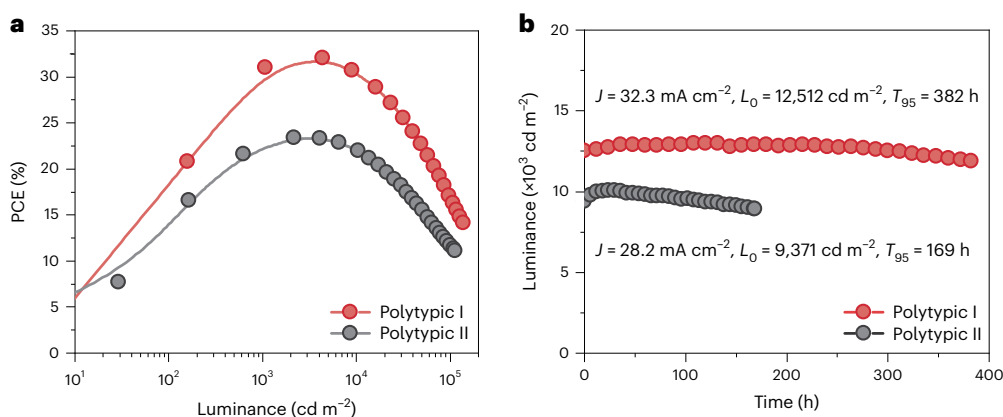
Fig. 4 | PCE and lifetime tests of QD-LED devices. a, Dependence of PCE on the luminance of QD-LEDs. **b**, T_{95} operational lifetime tests of QD-LEDs.

(BFP) imaging and angle-dependent photoluminescence spectroscopy to measure the in- and out-of-plane dipole proportions in the QD films (Supplementary Figs. 9 and 10; see Methods for details). From first principles, the bounds are as follows: the proportion should be 67% for completely isotropic emitters, whereas it can approach 100% for completely directional emitters. We obtained an experimental value of 69% for films based on polytypic II QDs (Fig. 2d and Supplementary Figs. 10–13). By contrast, polytypic I QD films exhibit an in-plane dipole proportion of 79% (Fig. 2d and Supplementary Figs. 10, 11, 14 and 15). The difference in in-plane dipole proportions originates from the different crystallography orientations of polytypic I (uniformly) and II (randomly) QD films.

Device fabrication and performance

We used the polytypic QDs to fabricate bottom-emitting LEDs adopting an ITO/PEDOT:PSS/TFB/QDs/ZnMgO/Al architecture (Fig. 3b inset and Supplementary Fig. 16; see Methods for definitions)[3]. All functional layers, except ITO and aluminium, are fabricated using solution-processing methods. Transfer matrix calculations are used to evaluate the impact of the in-plane dipole proportion on the out-coupling efficiency of these QD-LEDs (Supplementary Figs. 17–21). In general, maximum EQEs of 30.5% and 48.3% are obtained in LEDs using isotropic QDs (that is, with an in-plane dipole proportion of 67%) and ideal directional light-emitting QDs (that is, with an in-plane dipole proportion of 100%, Fig. 3a), respectively. Increasing in-plane dipole proportions from 69% to 79% enables an increment in theoretical EQE from 31.5% to 36.6% while keeping all other parameters constant.

Experimentally, thanks to the near-unity photoluminescence quantum yield (PLQY) (Supplementary Table 1; see Methods for details) and enhanced out-coupling, the EQE of our polytypic I QD-LEDs exceeds 30% across the 1,000–120,000 cd m^{-2} range at low biases (Fig. 3c and Supplementary Fig. 22; see Methods for details), reaching a peak and average value of 35.6% and 34.2%, respectively (Fig. 3d, 30 samples per class of QDs), which are the highest values reported among QD-LEDs. The device certified at National Institute of Metrology of China shows a peak EQE of 34% (Supplementary Fig. 23), which is close to the average peak EQE observed in the laboratory. We obtained a maximum EQE of 26.2% (Fig. 3c) in polytypic II QD-LEDs. It is worth noting that different in-plane dipole proportions only affect the light out-coupling efficiency; the angular distribution profiles of electroluminescence remain the same for polytypic I and II QDs (Supplementary Fig. 24).

The efficient charge injection enables a brightness of >57,000 cd m^{-2} at a low driving voltage of 3 V. The devices achieve a power conversion efficiency (PCE) of 32% (Fig. 4a; see Methods for details), 1.4-times higher than that in devices made using polytypic II QDs and 1.5-times higher than the highest PCE of

previously reported QD-LEDs[3]. The devices maintain a high PCE of >20% across the brightness range of 100 to 70,000 cd m^{-2}, the luminance range required for flat-panel displays and general lighting applications.

Device lifetime measurements

The reference polytypic II QD-LEDs show a T_{95} operational lifetime (defined as the time for the luminance to decrease to 95% of the initial luminance) of ~169 h at 9,400 cd m^{-2}, ~10,800 h at 1,000 cd m^{-2} and ~780,000 h at 100 cd m^{-2} (Fig. 4b and Supplementary Fig. 25). The stability of polytypic I QD-LEDs benefits from modest heat generation and a low driving voltage associated with the high PCE. The polytypic I QD-LEDs show a T_{95} of ~382 h at 12,500 cd m^{-2}, corresponding to ~40,900 h at 1,000 cd m^{-2} or ~3,000,000 h at 100 cd m^{-2} (Fig. 4b and Supplementary Fig. 25), a record among solution-processed LEDs, including QDs, perovskites and organic dyes (Supplementary Table 2).

Conclusion

We report the syntheses of polytypic QDs and introduce more ionic content into the WZ phase to increase the permanent dipole moment, allowing strong dipole–dipole interactions and uniform orientation of QDs. Meanwhile, the ZB phase helps lift the LH and HH degeneracy and enables directional light emission. As a result, we increase photon out-coupling efficiency without compromising the internal quantum efficiency, and achieve a record EQE of 35.6% in laboratory and a certified EQE of 34%. These devices can be continuously operated with an initial brightness of 1,000 cd m^{-2} for ~4.5 years with minimal (5%) performance loss. We expect this strategy can be expanded to blue and green colour QDs with proper materials engineering.

Online content

Any methods, additional references, Nature Portfolio reporting summaries, source data, extended data, supplementary information, acknowledgements, peer review information; details of author contributions and competing interests; and statements of data and code availability are available at https://doi.org/10.1038/s41566-023-01344-4.

References

1. Shirasaki, Y., Supran, G. J., Bawendi, M. G. & Bulović, V. Emergence of colloidal quantum-dot light-emitting technologies. *Nat. Photonics* **7**, 13–23 (2013).
2. Dai, X. et al. Solution-processed, high-performance light-emitting diodes based on quantum dots. *Nature* **515**, 96–99 (2014).
3. Shen, H. et al. Visible quantum dot light-emitting diodes with simultaneous high brightness and efficiency. *Nat. Photonics* **13**, 192–197 (2019).

4. Won, Y. H. et al. Highly efficient and stable InP/ZnSe/ZnS quantum dot light-emitting diodes. *Nature* **575**, 634–638 (2019).
5. Kim, T. et al. Efficient and stable blue quantum dot light-emitting diode. *Nature* **586**, 385–389 (2020).
6. Deng, Y. Z. et al. Solution-processed green and blue quantum-dot light-emitting diodes with eliminated charge leakage. *Nat. Photonics* **16**, 505–511 (2022).
7. Brutting, W., Frischeisen, J., Schmidt, T. D., Scholz, B. J. & Mayr, C. Device efficiency of organic light-emitting diodes: progress by improved light out-coupling. *Phys. Status Solidi a* **210**, 44–65 (2013).
8. Scott, R. et al. Directed emission of CdSe nanoplatelets originating from strongly anisotropic 2D electronic structure. *Nat. Nanotechnol.* **12**, 1155–1160 (2017).
9. Kim, W. D. et al. Pushing the efficiency envelope for semiconductor nanocrystal-based electroluminescence devices using anisotropic nanocrystals. *Chem. Mater.* **31**, 3066–3082 (2019).
10. Kumar, S. et al. Anisotropic nanocrystal superlattices overcoming intrinsic light outcoupling efficiency limit in perovskite quantum dot light-emitting diodes. *Nat. Commun.* **13**, 2106 (2022).
11. Cunningham, P. D. et al. Assessment of anisotropic semiconductor nanorod and nanoplatelet heterostructures with polarized emission for liquid crystal display technology. *ACS Nano* **10**, 5769–5781 (2016).
12. Gao, Y., Weidman, M. C. & Tisdale, W. A. CdSe nanoplatelet films with controlled orientation of their transition dipole moment. *Nano Lett.* **17**, 3837–3843 (2017).
13. Nam, S., Oh, N., Zhai, Y. & Shim, M. High efficiency and optical anisotropy in double-heterojunction nanorod light-emitting diodes. *ACS Nano* **9**, 878–885 (2015).
14. Cassette, E. et al. Colloidal CdSe/CdS dot-in-plate nanocrystals with 2D-polarized emission. *ACS Nano* **6**, 6741–6750 (2012).
15. Wang, Y., Pu, C., Lei, H., Qin, H. & Peng, X. CdSe@CdS dot@platelet nanocrystals: controlled epitaxy, monoexponential decay of two-dimensional exciton, and nonblinking photoluminescence of single nanocrystal. *J. Am. Chem. Soc.* **141**, 17617–17628 (2019).
16. Cho, K. S., Talapin, D. V., Gaschler, W. & Murray, C. B. Designing PbSe nanowires and nanorings through oriented attachment of nanoparticles. *J. Am. Chem. Soc.* **127**, 7140–7147 (2005).
17. Tang, Z., Zhang, Z., Wang, Y., Glotzer, S. C. & Kotov, N. A. Self-assembly of CdTe nanocrystals into free-floating sheets. *Science* **314**, 274–278 (2006).
18. Tang, Z. Y., Kotov, N. A. & Giersig, M. Spontaneous organization of single CdTe nanoparticles into luminescent nanowires. *Science* **297**, 237–240 (2002).
19. Talapin, D. V., Shevchenko, E. V., Murray, C. B., Titov, A. V. & Kral, P. Dipole–dipole interactions in nanoparticle superlattices. *Nano Lett.* **7**, 1213–1219 (2007).
20. Nann, T. & Schneider, J. Origin of permanent electric dipole moments in wurtzite nanocrystals. *Chem. Phys. Lett.* **384**, 150–152 (2004).
21. Yeh, C. Y., Lu, Z. W., Froyen, S. & Zunger, A. Zinc-blende-wurtzite polytypism in semiconductors. *Phys. Rev. B* **46**, 10086–10097 (1992).
22. Park, Y.-S., Lim, J. & Klimov, V. I. Asymmetrically strained quantum dots with non-fluctuating single-dot emission spectra and subthermal room-temperature linewidths. *Nat. Mater.* **18**, 249–255 (2019).
23. Segarra, C., Rajadell, F., Climente, J. I. & Planelles, J. Influence of polytypism on the electronic structure of CdSe/CdS and CdSe/CdSe core/shell nanocrystals. *J. Phys. Chem. C* **121**, 6386–6392 (2017).
24. Shim, M. & Guyot-Sionnest, P. Permanent dipole moment and charges in colloidal semiconductor quantum dots. *J. Chem. Phys.* **111**, 6955–6964 (1999).
25. Marcato, T., Krumeich, F. & Shih, C. J. Confinement-tunable transition dipole moment orientation in perovskite nanoplatelet solids and binary blends. *ACS Nano* **16**, 18459–18471 (2022).
26. Song, Y. et al. Enhanced emission directivity from asymmetrically strained colloidal quantum dots. *Sci. Adv.* **8**, 8 (2022).
27. Efros, A. L. et al. Band-edge exciton in quantum dots of semiconductors with a degenerate valence band: dark and bright exciton states. *Phys. Rev. B* **54**, 4843–4856 (1996).
28. Fan, F. et al. Continuous-wave lasing in colloidal quantum dot solids enabled by facet-selective epitaxy. *Nature* **544**, 75–79 (2017).

Methods

Materials

Cadmium oxide (CdO, 99.99%), zinc acetate ((Zn(OAc)$_2$, 99.99%), sulfur (99.99%, powder), 1-octadecene (ODE, 90%), oleic acid (OA, 90%), trioctylphosphine (TOP, 97%), selenium (99.99%, powder) chlorobenzene (99%), zinc acetate dihydrate (Zn(OAc)$_2$·2H$_2$O, 99.999%), magnesium acetate tetrahydrate (Mg(OAc)$_2$·4H$_2$O, 99.9%), tetramethylammonium hydroxide pentahydrate (99%) and dimethyl sulfoxide (99.7%) were purchased from Sigma-Aldrich. Poly(ethylenedioxythiophene):polystyrene sulphonate (PEDOT:PSS, AI4083) was purchased from Heraeus Deutschland GmbH & Co. KG. Poly(9,9-dioctylfluorene-co-N-(4-(3-methylpropyl))-diphenylamine) (TFB) was purchased from American Dye Source. The above reagents were used as received.

Preparation of precursors

Zinc precursor: a mixture of Zn(OAc)$_2$ (12 mmol), OA (6 ml) and ODE (24 ml) was loaded into a 100 ml flask, heated to 120 °C and exhausted for 10 min, followed by heating up to 310 °C and boiling for 20 min. Selenium precursor: 5 mmol selenium powder was mixed with 10 ml TOP and stirred to obtain a clear solution. Se–S precursor: 2.5 mmol selenium powder, 2.5 mmol sulfur powder and 10 ml TOP were all mixed together, and stirred to get a clear solution. Sulfur precursor: 5 mmol sulfur powder was mixed with 10 ml TOP and stirred to obtain a clear solution.

Synthesis of polytypic II (Cd$_{1-x}$Zn$_x$Se/ZnSe/ZnSeS)

CdO (1.4 mmol), Zn(OAc)$_2$ (1.8 mmol), ODE (20 ml) and OA 10 ml were mixed in a 100 ml three-necked flask, the temperature was raised to 120 °C, and the flask was exhausted under nitrogen flow for 10 min. After that, the temperature was raised to 310 °C and 6 ml of selenium precursor was rapidly injected, and the reaction was performed for 60 min to grow ZnCdSe cores. After that, the temperature was lowered to 270 °C, 4 ml of zinc precursor was added dropwise for 10 min, followed by 4 ml of selenium precursor, and the reaction was continued for 20 min to grow a ZnSe shell. To grow the ZnSeS shell layer, the temperature was raised to 290 °C, and 4 ml of zinc precursor was added dropwise to react for 10 min, and then 4 ml of Se-S precursor was added dropwise to react for 20 min. The temperature was quickly lowered to room temperature after completion.

Synthesis of polytypic I (Cd$_{1-x}$Zn$_x$Se/ZnSe/ZnSeS/ZnS)

The synthesis of ZnCdSe core was the same as polytypic II. After that, the temperature was lowered to 290 °C, 4 ml of zinc precursor was added dropwise for 10 min, followed by 4 ml of Se-S precursor, and the reaction was continued for 20 min to grow a ZnSeS shell. When coating the ZnS shell layer, the temperature was raised to 310 °C, 4 ml of zinc precursor was added dropwise for 10 min, and then 4 ml of sulfur precursor was added dropwise for 10 min to grow a ZnS shell, and the temperature was quickly lowered to room temperature after completion.

Back-focal plane imaging and fitting

The QD films were made by spin-coating the CQDs in n-octane dispersions onto a 0.15 nm cover slide. The back-focal plane images of emission of the QD film are collected by an objective lens (Nikon CFI Plan Apochromat Lambda 100× oil, numerical aperture of 1.45), two coupled 200-mm focal planoconvex lenses, and a scientific complementary metal–oxide–semiconductor camera (TUCSEN Dhyana 400BSI v.2). The two lenses were placed on the back optical path of the objective lens and projected the BFP image of the objective lens onto the camera. A polarizer (Thorlabs CCM1-PBS251) was used to generate the polarization image of the BFP, and a bandpass filter (Semrock FF02-641/75-25) was used to filter out the excitation and noise light.

In this technique, the transition dipole moments are projected to the directions parallel and perpendicular to the substrate planes (that is, in-plane and out-of-plane, respectively), and we can obtain the in-plane

dipole proportion by fitting the data[12,26,29,30]. As photon emission perpendicular to the dipole moment is the strongest, photon emission from the in-plane dipoles is more likely to be extracted. By contrast, most radiation from the out-of-plane dipoles is trapped in the substrate. A high proportion of in-plane dipole is therefore desired for enhancing light-coupling. For an isotropic QD emitter, the dipole moments can be projected equally to three dimensions in the space; two exist in the substrate plane, and the left one is along the perpendicular direction[26].

The BFP image fitting methods are the same as our previous work[26], and here we give the key equations used for fitting. The structure used for the fitting is shown in Supplementary Fig. 9. The Poynting vector of the plane in the glass layer can be written as a function of in-plane dipole proportion (ip%).

$$S = \text{ip}\% \times (S_{\text{ip},s} + S_{\text{ip},p}) + (1 - \text{ip}\%) \times S_{\text{op},p}$$

It can be written as components of p- and s-polarization.

$$S_p = \text{ip}\% \times S_{\text{ip},p} + (1 - \text{ip}\%) \times S_{\text{op},p}$$

$$S_s = \text{ip}\% \times S_{\text{ip},s}$$

By fitting the measured p- and s- direction of the polarization intensity profile of the BFP image, the in-plane dipole proportion can be obtained. The bases used in fitting shown in Supplementary Fig. 9 insets are calculated by the transfer matrix method.

GIWAXS measurements

GIWAXS data were collected at SAXS beamline BL16B1 of the Shanghai Synchrotron Radiation Facility, China, and analysed by SGTools[31].

Angle-resolved spectroscopy measurements

Angle-resolved spectra were measured by an angle-resolved spectrum system (R1 Ideaoptics, China). A hemispherical lens was placed on the sample with refractive index-matched immersion oil dripping in between to eliminate the air layer.

Synthesis of ZnMgO nanoparticles

Zn$_{0.90}$Mg$_{0.10}$O nanoparticles were synthesized by a solution-precipitation process. A solution of Zn(OAc)$_2$·2H$_2$O (2.7 mmol) and Mg(OAc)$_2$·4H$_2$O (0.3 mmol) in dimethyl sulfoxide (30 ml) with tetramethylammonium hydroxide pentahydrate (5 mmol) in ethanol (10 ml) were mixed and stirred for 1 h in ambient air. Then Zn$_{0.90}$Mg$_{0.10}$O nanoparticles were washed and dispersed in ethanol.

Fabrication of QD-LEDs

The patterned ITO glass substrates were ultrasonically cleaned with detergent, deionized water, acetone and isopropanol in sequence for 15 min, then dried and treated with ultraviolet ozone for 15 min; PEDOT:PSS was spin-coated at 5,500 r.p.m. for 40 s on the ITO substrate and annealed at 150 °C for 15 min. These substrates were then transferred into a N$_2$-filled glovebox to deposit the subsequent layers. TFB (8 mg ml^{-1} in chlorobenzene, 3,000 r.p.m. for 30 s), QD (15 mg ml^{-1} in octane, 2,000 r.p.m. for 40 s) and ZnMgO (25 mg ml^{-1} in ethanol, 2,000 r.p.m. for 30 s) were sequentially spin-coated. After spin-coating TFB and ZnMgO, they were annealed at 110 °C and 145 °C for 30 min, respectively. When fabricating devices in summer, the spin-coating conditions are as follows: PEDOT:PSS (5,000 r.p.m.), TFB (18 mg ml^{-1}, 3,000 r.p.m.), QD (20 mg ml^{-1}, 2,500 r.p.m.) and ZnMgO (30 mg ml^{-1}, 2,500 r.p.m.). Finally, a high-vacuum chamber (~5 × 10^{-6} mbar) was used to thermally deposit the aluminium cathode (100 nm) (Supplementary Fig. 26).

Transfer matrix method

The power distribution of QD-LEDs is calculated by the transfer matrix method, which has been elaborated on in the previous articles[32,33].

Here we skip the derivation and show only the basic principle and some details. The multilayer QD-LED structure and refractive index of all layers are shown in Supplementary Figs. 17–20, the electric fields at interfaces satisfy the relationship:

$$\begin{pmatrix} E_1^+ \\ 0 \end{pmatrix} = I_1 L_2 \cdots I_{i-1} L_i \begin{pmatrix} E_i^+ \\ E_i^- \end{pmatrix} \qquad (i \le s),$$

$$\begin{pmatrix} E_i^+ \\ E_i^- \end{pmatrix} = L_i I_{i+1} \cdots L_{M-1} I_M \begin{pmatrix} 0 \\ E_M^- \end{pmatrix} \qquad (i > s).$$

where the +(−) represents upward (downward) propagation; I is the refractive matrix; L is the phase matrix; s is the serial number of the emitter layer; and M is the total number of interfaces. The electric fields of every interface can be easily calculated by the above two matrix relations and the following one.

$$\begin{pmatrix} E_{s+1}^+ \\ E_{s+1}^- \end{pmatrix} - \begin{pmatrix} E_s^+ \\ E_s^- \end{pmatrix} = \begin{pmatrix} A^+ \\ A^- \end{pmatrix}$$

where the A is the source term listed in Supplementary Table 3. Then the z-directional Poynting vector of each interface can be calculated from the electric fields:

$$S_i = \begin{cases} \mathrm{Real}\{n_i \cos\phi_i (E_i^+ + E_i^-)^* (E_i^+ - E_i^-)\} & \text{(TE)} \\ \mathrm{Real}\{n_i \cos\phi_i^* (E_i^+ + E_i^-)^* (E_i^+ - E_i^-)\} & \text{(TM)} \end{cases}$$

where $\cos\phi_i = k_{zi}/k_i$. The power fluxes are the integral of the Poynting vector at every interface.

$$P_i = \int\limits_0^\infty \frac{2\pi}{n_s k_{zs}^2} S_i k_r dk_r$$

The outcoupling power P_{out} is part of P_1, which is divided according to the in-plane wave vector k_r ($0 < k_r < k_0$, where $k_0 = 2\pi/\lambda$ is the vacuum wave vector). The total power $P_{\mathrm{tot}} = P_s + P_{s+1}$, and the outcoupling efficiency is obtained from the ratio of P_{out} to P_{tot}. The power of other modes is obtained by dividing the P_i of different interfaces according to k_r.

Refractive index measurements
The refractive index of films in QD-LED was measured by an ellipsometer (SE-VM-L Spectroscopic Ellipsometer, Wuhan Eoptics Technology).

DFT computation
Calculations of the wave functions of band-edge energy levels are performed using the SIESTA code[34] with GGA-PBE[35] exchange-correlation functional and DZP basis sets. The plain wave cutoff energy of the grid is set to 300 Ry (150 Ry in geometric optimization). Geometric optimization is performed using the conjugate gradient method, with maximum atomic displacement set to 0.1 Å. The pseudopotentials are generated with the included ATOM program[34]. The models used are sphere-shaped core–shell CdSe/ZnSe QDs, with an overall diameter of 5 nm and a core diameter of 3 nm. For the pure WZ QDs, the cell is first expanded and cut to a spherical shape, and the surface is passivated with pseudo-hydrogen to maintain charge balance. For polytypic dots, the WZ layer in the centre is constructed first and then ZB parts are constructed on two sides. The thickness of the WZ layer is 3.6 nm.

We used the Vienna Ab initio Simulation Package[36] to perform the Bader charge calculations. The Perdew–Burke–Ernzerhof functional[35] and the screened Heyd–Scuseria–Ernzerhof (HSE06) hybrid functional[37,38] were adopted for the exchange-correlation functional. We used the cutoff energy of 400 eV with the energy and force convergence tolerance of 10^{-5} eV and 0.02 eV Å^{-1}, respectively. We used the code developed by Henkelman group to do the Bader charge analysis[39].

Calculations for the dipole moments of the 8-nm-diameter QDs were performed using the CP2K package[40]. The cut-off was set to 400 Ry.

Dielectric spectroscopy measurements and fitting
Dielectric spectra were measured by an impedance analyser (Keysight E4990A Impedance Analyzer, 20 Hz to 120 MHz) with a liquid test fixture (Keysight 16452A Liquid test fixture). QDs are dispersed in decalin and measured at a 1.0 V amplitude from 10^3 to 10^7 Hz. The complex dielectric (ε) consists of a real part (ε') and an imaginary part (ε''). The former represents the ability of a material to store energy in an external electric field, whereas the latter represents the ability of dissipation. In the absence of an electric field, the direction of the permanent dipole moment is random, so there is no polarization. The electric field E exercises a torque on the electric dipole, which rotates to align with the electric field, resulting in directional polarization (Fig. 2a, inset). This polarization increases the ability of the dielectric to store energy, while the friction accompanying the dipole orientation increases the dielectric loss. The dipole rotation causes both ε' and ε'' variation at the relaxation frequency. The contribution of dipolar relaxation to ε is $\varepsilon_d(\omega)$. The frequency response of particles with a permanent dipole moment is given by the Debye relaxation[24,41].

$$\varepsilon_d(\omega) = \frac{\Delta \varepsilon_d}{1 + i\omega\tau_d}$$

where $\Delta\varepsilon_d = n\mu^2/(3kT\varepsilon_0)$ is the contribution to the ε in the low-frequency limit; $\tau_d = 4\pi\eta a^3/kT$ is the dipolar relaxation time; n is the nanoparticle number density; k is the Boltzmann constant; T is the absolute temperature; η is the viscosity of the solvent; and a is the hydrodynamic radius; ε' is fitted to the real part of Debye relaxation and an electrode polarization term of the form $A\omega^{-3/2}$, and ε'' is fitted to the imaginary part plus a conductivity term, B/ω, where A and B are constants.

Detailed calculations of the EQE
The EQE is calculated according to the formula below by assuming that the emission obeys a Lambertian profile[42,43],

$$\eta_{\mathrm{EQE}} = \frac{\pi L e}{K_m hcJ} \frac{\int I(\lambda)\lambda d\lambda}{\int I(\lambda)V(\lambda)d\lambda},$$

where e is the electron charge, h is the Planck's constant, c is the velocity of light and $K_m = 683$ lm W^{-1} is the maximum luminous efficacy[42,43]. The current density J is measured from the current density–voltage characteristics using an Agilent 4155C semiconductor parameter analyser with a calibrated Newport silicon diode under ambient conditions. $I(\lambda)$ is the relative electroluminescence intensity at wavelength λ, obtained from the electroluminescence spectrum measured with an Ocean Optics spectrometer (USB2000, relative irradiance mode) supplied by a Keithley 2400 source meter, and $V(\lambda)$ is the normalized photonic spectral response function; L is the total luminance, which is calibrated using a Minolta luminance meter (LS-100) and Photo Research spectroradiometer (PR735 or PR650) for the two different device setups.

Detailed calculations of PCE
The PCE is calculated according to the following formula:

$$\mathrm{PCE} = \frac{\text{radiation power}}{\text{input power}}.$$

The radiation power can be calculated by integrating the product of photon flux and detected optical intensity.

$$\text{radiation power} = \int \frac{hc}{\lambda} I_{\mathrm{det}}(\lambda) d\lambda,$$

where $I_{\det}(\lambda)$ is the detected optical intensity at wavelength between λ and $\lambda + d\lambda$, h is Plank's constant, q is electronic charge and c is speed of light in vacuum. Input power can be described as:

$$\text{input power} = VI_{\text{current}},$$

where V and I_{current} are the driving voltage and current, respectively.

$$I_{\text{current}} = q \times \frac{\int I_{\det}(\lambda)d\lambda}{\text{EQE}}.$$

$\int I_{\det}(\lambda)d\lambda$ is the number of photons produced per unit time, which is equal to the number of consumed electrons per unit time; $\frac{\int I_{\det}(\lambda)d\lambda}{\text{EQE}}$ is the total number of electrons per unit time. So PCE can be expressed as:

$$\text{PCE} = \frac{hc\int \frac{I_{\det}(\lambda)}{\lambda}d\lambda}{qV\int I_{\det}(\lambda)d\lambda}\text{EQE}.$$

The PCE of previously reported devices is calculated by assuming that the electroluminescence spectra are symmetric, and average photon energy is equivalent to that of the photons with the highest photoluminescence count.

$$\text{PCE} = \frac{hc}{qV\lambda}\text{EQE},$$

where λ_0 is the central wavelength for electroluminescence, h is Plank's constant, q is electronic charge, V is voltage, and c is speed of light in vacuum.

Measurement of PLQY
The PLQY of QD solution and solid-state films were measured in an integrating sphere by an absolute PLQY measurement system (Ocean Optics ISP-50-8-I). The optical density of the QD solution samples were all between 0.02 and 0.05 at the excitation wavelength. The solid-state QD films were prepared by spin-coating on pre-cleaned 1.0×1.0 cm^2 glass substrates.

Data availability
The data that support the findings of this study are available from the corresponding authors on reasonable request. They are also available at figshare: https://doi.org/10.6084/m9.figshare.24236629. Source Data are provided with this paper.

References
29. Taminiau, T. H., Karaveli, S., van Hulst, N. F. & Zia, R. Quantifying the magnetic nature of light emission. *Nat. Commun.* **3**, 979 (2012).
30. Schuller, J. A. et al. Orientation of luminescent excitons in layered nanomaterials. *Nat. Nanotechnol.* **8**, 271–276 (2013).
31. Zhao, N., Yang, C., Bian, F., Guo, D. & Ouyang, X. SGTools: a suite of tools for processing and analyzing large data sets from in situ X-ray scattering experiments. *J. Appl. Crystallogr.* **55**, 195–203 (2022).
32. Benisty, H., Stanley, R. & Mayer, M. Method of source terms for dipole emission modification in modes of arbitrary planar structures. *J. Opt. Soc. Am. A* **15**, 1192–1201 (1998).
33. Mitsas, C. L. & Siapkas, D. I. Generalized matrix-method for analysis of coherent and incoherent reflectance and transmittance of multilayer structures with rough surfaces, interfaces, and finite substrates. *Appl. Optics* **34**, 1678–1683 (1995).
34. Soler, J. M. et al. The SIESTA method for ab initio order-*N* materials simulation. *J. Phys. Condens. Matter* **14**, 2745–2779 (2002).
35. Perdew, J. P., Burke, K. & Ernzerhof, M. Generalized gradient approximation made simple. *Phys. Rev. Lett.* **77**, 3865–3868 (1996).
36. Kresse, G. & Furthmüller, J. Efficient iterative schemes for ab initio total-energy calculations using a plane-wave basis set. *Phys. Rev. B* **54**, 11169–11186 (1996).
37. Heyd, J., Scuseria, G. E. & Ernzerhof, M. Hybrid functionals based on a screened Coulomb potential. *J. Chem. Phys.* **118**, 8207–8215 (2003).
38. Paier, J. et al. Screened hybrid density functionals applied to solids. *J. Chem. Phys.* **124**, 154709 (2006).
39. Henkelman, G., Arnaldsson, A. & Jónsson, H. A fast and robust algorithm for Bader decomposition of charge density. *Comput. Mater. Sci.* **36**, 354–360 (2006).
40. Kühne, T. D. et al. CP2K: an electronic structure and molecular dynamics software package—quickstep: efficient and accurate electronic structure calculations. *J. Chem. Phys.* **152**, 194103 (2020).
41. Kortschot, R. J., van Rijssel, J., van Dijk-Moes, R. J. A. & Erné, B. H. Equilibrium structures of PbSe and CdSe colloidal quantum dots detected by dielectric spectroscopy. *J. Phys. Chem. C* **118**, 7185–7194 (2014).
42. Okamoto, S. et al. Simple measurement of quantum efficiency in organic electroluminescent devices. *Jpn. J. Appl. Phys.* **40**, L783–L784 (2001).
43. Forrest, S. R., Bradley, D. D. C. & Thompson, M. E. Measuring the efficiency of organic light-emitting devices. *Adv. Mater.* **15**, 1043–1048 (2003).

Author contributions
F.J.F. and H.B.S. conceptualized the work and designed the experiments. H.B.S., F.J.F., J.F.D. and E.H.S. supervised the project. H.Y.X. and Y.S. performed the BFP and dielectric spectroscopy experiments and fitting, as well as the transfer matrix computations. P.H.Z., J.J.S and Y.G. synthesized the materials, fabricated the devices and collected the performance data of the QD-LEDs. J.X., S.C.F. and O.V. performed DFT calculations. Z.J.Z. contributed to dielectric spectroscopy experiments. C.M.Y., Y.F.H. and J.L. performed GIWAXS measurements and analyses. H.Y.X., F.J.F., H.B.S., J.M.P. and E.H.S. wrote the paper. All authors contributed to the scientific discussion about this work.

Competing interests
Patents related to directional light emission QDs will be submitted.